Dielectric properties of graphene/MoS$_2$ heterostructures from *ab initio* calculations and electron energy-loss experiments

Michael J. Mohn,[1, *] Ralf Hambach,[1, 2] Philipp Wachsmuth,[1] Christine Giorgetti,[2, 3] and Ute Kaiser[1]

[1]*Electron Microscopy Group of Materials Science, Ulm University, Albert-Einstein-Allee 11, 89081 Ulm, Germany*
[2]*Laboratoire des Solides Irradiés, Ecole Polytechnique, CNRS, CEA, Université Paris-Saclay, 91128 Palaiseau, France*
[3]*European Theoretical Spectroscopy Facility, 91128 Palaiseau, France*

High-energy electronic excitations of graphene and MoS$_2$ heterostructures are investigated by momentum-resolved electron energy-loss spectroscopy in the range of 1 to 35 eV. The interplay of excitations on different sheets is understood in terms of long-range Coulomb interactions and simulated using a combination of *ab initio* and dielectric model calculations. In particular, the layered electron-gas model is extended to thick layers by including the spatial dependence of the dielectric response in the direction perpendicular to the sheets. We apply this model to the case of graphene/MoS$_2$/graphene heterostructures and discuss the possibility of extracting the dielectric properties of an encapsulated monolayer from measurements of the entire stack.

I. INTRODUCTION

A transmission electron microscope (TEM), equipped with a spectrometer to analyze the energy of scattered electrons, is an ideal tool to investigate electronic excitations in solids, nanostructures, and two-dimensional (2D) materials. Typical setups for electron energy-loss spectroscopy (EELS) in TEMs cover energy ranges starting from a few eV up to keV and allow for variable spatial resolution down to individual atoms. If the scattering angle is recorded, one can study the change in the excitation energy with the momentum transferred to the sample. This energy dispersion helps to reveal the nature of excitations in the sample and to distinguish, e.g., plasmons from interband transitions[1] and Wannier-Mott excitons from Frenkel excitons.[2,3] Such momentum-resolved EELS studies have been successfully applied to investigate excitations in bulk materials[4–7] and nanostructures.[8–10] More recently, 2D materials like graphene (G), hexagonal boron nitride (hBN), and transition metal dichalcogenides (TMDs) have also been studied.[11–15]

TEM studies on atomically thin layers are very challenging, as they suffer from beam-induced damage and contamination, which alter the recorded signal. For the investigation of defect-free graphene with TEM or TEM-EELS, the energy of the primary electrons has to be reduced below the knock-on threshold of about 80 kV.[16] Many other low-dimensional materials are even more sensitive,[17,18] raising increasing interest in low-voltage electron microscopy.[19–22] Additionally, the sample may be sandwiched between two protective graphene layers, which can increase the radiation hardness by several orders of magnitude.[23,24] In this case, the signal from the graphene sheets has to be removed afterwards: In aberration-corrected TEM imaging, Fourier filtering may be applied,[23,25] and in core-loss EELS experiments, the relevant signals are sufficiently separated. For low-loss EELS, however, excitations on different layers are coupled, and it is no longer clear how to extract the spectrum of the sandwiched layer.

These complications hold for arbitrary van der Waals heterostructures, which present growing interest due to their adjustable electronic properties[26–30] and potential applications.[31–34] In order to predict their dielectric properties, much work has been dedicated to rigorous and accurate calculations using time-dependent density-functional theory (TDDFT) and many-body perturbation theory (see Refs. [35–37] for a recent review). These calculations require a large computational effort for each of the many possible heterostructures. Thus, it is very useful to complement *ab initio* simulations with less accurate but more efficient model calculations, such as a layered electron-gas (LEG) model[38] or a quantum-electrostatic heterostructure (QEH) model,[39] or by assuming the separability of the wavefunctions into in-plane and out-of-plane components.[40,41]

In this paper, we evaluate the accuracy of different dielectric models for the momentum-dependent dielectric response of heterostructures using *ab initio* calculations and corresponding EELS experiments. Although the LEG model has been successfully applied for the simulation of multilayer graphene,[42,43] we demonstrate its limitations for heterostructures made of thick layers, like MoS$_2$, and introduce model calculations that take a vertical extension of the sheet into account. As a prototypical example, we calculate electron energy-loss spectra of a G/MoS$_2$/G sandwich starting from the dielectric response of its building blocks, graphene and 1H-MoS$_2$. Finally, we address the reverse process of extracting the dielectric response of the encapsulated layer from measurements of the G/MoS$_2$/G heterostructure and evaluate prospects of the sandwiching technique in TEM-EELS.

This paper is structured as follows: First we review our experimental and theoretical methods used to study momentum-resolved electron energy-loss spectra of single- and multilayer systems (Sec. II). Then we compare our experimental TEM-EELS results for a bare 1H-MoS$_2$ monolayer (Sec. III A) with results obtained for a protected monolayer, i.e., a G/MoS$_2$/G sandwich (Sec. III B). To understand the influence of the graphene sheets on the dielectric response of the monolayer, different model calculations for the momentum-resolved spectra of van der Waals heterostructures are presented (Sec. III C): Extending the well-known LEG model, we propose two models accounting for a finite thickness of the constituent 2D layers [the building-block approach (BBA) and the in-plane homogeneous model (IPH)] and assess their accuracy for the prototypical case of bulk MoS$_2$. Finally, these models are used to simulate the energy-loss spectra of the G/MoS$_2$/G heterostruc-

ture and discuss the applicability of the sandwiching technique in TEM-EELS (Sec. III D).

II. METHODS

A. Experiments

Our TEM-EELS measurements were performed at an acceleration voltage of $40\,\mathrm{kV}$ using the "SALVE I" Zeiss Libra-200-based TEM prototype,[12,21] which is equipped with a monochromator and an Ω-type in-column energy filter. All TEM samples were produced by mechanical exfoliation of graphene or MoS_2 and a subsequent transfer to holey carbon TEM grids. G/MoS_2/G sandwich samples have been produced by multiple transfers of graphene and MoS_2 monolayers.[23] The incident electron beam is oriented perpendicular to the 2D layers, illuminating a freestanding sample area of about $200-400$ nm diameter. We use the diffraction mode of the microscope and insert a slit aperture in the spectrometer entrance plane to select scattering angles along a certain crystallographic direction of the sample. A TEM holder with in-plane specimen rotation capability is used to bring the sample in the desired orientation (ΓM or ΓK). The energy filter disperses the electrons according to their energy along a direction perpendicular to the slit. In this manner, energy-loss spectra for different momentum transfers can be recorded simultaneously in an ω-q map, with energy and momentum resolutions of around 0.1 eV and $0.1\,\text{Å}^{-1}$ respectively.[12] For each ω-q map, a series of at least 100 images has been acquired for 1 to 1.5 s per frame on a 4096×4096 pixel complementary metal-oxide semiconductor (CMOS) camera. In postprocessing, the single acquisitions have been aligned, corrected for spectrometer distortions, and summed up. A detailed discussion of limiting factors for energy and momentum resolution can be found in Refs. 12 and 44. The software used for the analysis of the momentum-resolved EELS data is available online.[45]

By extracting spectra for different scattering angles θ from the ω-q map, we access information about the momentum-resolved inverse dielectric function $\varepsilon^{-1}(\boldsymbol{q}, E)$ of the sample via the recorded double-differential scattering cross section

$$\frac{\partial^2 \sigma}{\partial \Omega \partial E} \propto \frac{-1}{\bar{q}^2 + q_E^2} \operatorname{Im} \varepsilon^{-1}(\boldsymbol{q}, E). \tag{1}$$

Here, $\bar{q} \approx \frac{2\pi}{\lambda}\theta$, $q_E \approx \frac{2\pi}{\lambda}\frac{E}{2E_0}$, and $\boldsymbol{q} = \bar{\boldsymbol{q}} + q_E \boldsymbol{e}_z$ denote the in-plane, out-of-plane, and total momentum transfer, respectively. As the energy transfer E is small compared to the energy E_0 of the incident electrons, we have $q_E \ll \bar{q}$; that is, the total momentum transfer is nearly parallel to the 2D sample. We extract the energy-loss function $\mathrm{ELF}(\boldsymbol{q}, E) = -\operatorname{Im}\varepsilon^{-1}(\boldsymbol{q}, E)$ from the measured spectrum in Eq. (1) by correcting for the momentum and energy dependent prefactor and the finite width of the slit aperture. The ELF can be directly compared with corresponding calculations.

Note that the measured signal also includes a large contribution from unscattered electrons, which have a certain energy distribution around $E = 0$ eV. The largest part has been blocked

by a beam stop to protect the camera ($E \approx 0\,\mathrm{eV}$, $\bar{q} \approx 0\,\text{Å}^{-1}$). In order to separate the tails of this zero-loss peak (ZLP) from the inelastic signal, an additional measurement without the specimen was performed right after measuring each ω-q map. These reference spectra are shown as blue dotted curves throughout this paper.

B. First-principles calculations for monolayers

To compute the dielectric response of graphene and MoS_2 monolayers, we performed first-principles calculations using time-dependent density-functional theory:[46] First, the ground-state was computed with the plane-wave pseudopotential DFT code ABINIT[47] within the local-density approximation using norm-conserving Troullier-Martins pseudopotentials. For the plane-wave basis sets, energies of up to 30 Ha (graphene) and 40 Ha (MoS_2) have been used. Second, the independent-particle response χ^{KS} of noninteracting Kohn-Sham (KS) particles was calculated in linear-response approximation using the DP code.[48] Converged results were obtained using Monkhorst-Pack k-point grids with $59 \times 59 \times 1$ symmetric sampling points (graphene, ΓM) and $23 \times 23 \times 1$ shifted sampling points (MoS_2, ΓM) for the Brillouin zone integration. A supercell height L_z of twice the interlayer distance in bulk graphite and 2H-MoS_2 was sufficient to avoid interactions with artificial replicas of the monolayers. Note that for a periodic system, the microscopic response function $\chi^{\mathrm{KS}}(\boldsymbol{r}, \boldsymbol{r}', E)$ becomes a matrix $\chi^{\mathrm{KS}}_{\boldsymbol{G}\boldsymbol{G}'}(\boldsymbol{q}, E)$ in plane-wave representation. All three-dimensional reciprocal lattice vectors $\boldsymbol{G}$ and $\boldsymbol{G}'$ smaller than $G_{\mathrm{cut}} = 8\,\text{Å}^{-1}$ (graphene) and $G_{\mathrm{cut}} = 6\,\text{Å}^{-1}$ (MoS_2) have been taken into account. Third, the linear response χ of interacting electrons to an electron-beam induced perturbation was obtained in the random-phase approximation (RPA) by solving the matrix equation[46]

$$\chi = \chi^{\mathrm{KS}} + \chi^{\mathrm{KS}} v_{\mathrm{C}} \chi, \qquad v_{\mathrm{C}} = 4\pi|\boldsymbol{q} + \boldsymbol{G}|^{-2}, \tag{2}$$

where v_{C} denotes the classical Coulomb interaction between electrons. Its long-range part ($\boldsymbol{G} = \boldsymbol{0}$) gives rise to collective electronic excitations (plasmons), while the short-range part ($\boldsymbol{G} \neq \boldsymbol{0}$) is responsible for the so-called crystal local-field effects. Exchange and correlation effects are completely neglected in the response of the system. To avoid interactions between different supercells, Eq. (2) has been solved in mixed coordinates ($\bar{\boldsymbol{q}}, z$) using a plane-wave basis $e^{i\bar{\boldsymbol{q}}\boldsymbol{r}}$ for the in-plane direction and a real-space grid along the out-of-plane direction z.[49,50] Finally, the energy-loss function of the monolayer, normalized to unit area, was obtained in reciprocal space as

$$\mathrm{ELF}(\bar{\boldsymbol{q}}, E) = -L_z v_{\mathrm{C}}(\bar{\boldsymbol{q}}) \operatorname{Im} \chi_{\boldsymbol{00}}(\bar{\boldsymbol{q}}, E), \tag{3}$$

where we have restricted ourselves to in-plane momentum transfers, $\boldsymbol{q} = \bar{\boldsymbol{q}}$, inside the first Brillouin zone, $\bar{\boldsymbol{G}} = \bar{\boldsymbol{0}}$. In the literature, analogous TDDFT calculations for graphene[8,51,52] and MoS_2 monolayers[15,53] were performed with very similar results.

III. RESULTS AND DISCUSSION

A. Monolayer MoS$_2$

Before we discuss the momentum-resolved EELS signal of the full graphene and MoS$_2$ heterostructure, we compare our calculations and experiments for a monolayer of MoS$_2$. Our data complement a detailed EELS study on MoS$_2$ for small $\bar{q}$[14] as well as our previous work on graphene.[12] Figure 1(a) shows the calculated and measured energy-loss function of monolayer MoS$_2$ for in-plane momentum transfers up to $\bar{q} = 0.6\,\text{Å}^{-1}$ in the ΓM direction (see the Supplemental Material[54] (SM), Fig. S4, for a larger set of momentum transfers). For $\bar{q} = 0\,\text{Å}^{-1}$, large differences between theoretical and experimental data are observed. Like in the case of graphene, this can be explained by three reasons: First, due to the finite momentum resolution in experiment, the measured EEL spectra are actually a weighted average of rather different spectra with $\bar{q}$ values up to $0.1\,\text{Å}^{-1}$. A corresponding simulation shows the importance of the limited resolution for very small $\bar{q}$ (see the SM,[54] Section I B). Second, we observe additional peaks at low energy losses that are not present in the RPA *ab initio* calculations. Two features at around 2 and 3 eV have been reported by previous EELS experiments[14,55,56] and can be attributed to excitonic states.[36,57] Such excitonic effects are not included in the RPA approximation and have been investigated in detail for MoS$_2$ monolayers by solving the Bethe-Salpeter equation for vanishing[58,59] and finite $\bar{q}$.[60] Third, our experimental spectra show an additional peak at higher energies of about 23 eV. For graphene, a similar feature has been attributed to out-of-plane excitations[12] which are not taken into account by our in-plane calculations. For finite momentum transfers (0.3 and $0.6\,\text{Å}^{-1}$), we achieve relatively good agreement between the simulations and experiments regarding the position and intensity of the two most prominent peaks. With increasing $\bar{q}$, the peak above 10 eV shifts to higher energy and becomes more dominant in the spectrum. In analogy to similar peaks in graphite and graphene, we will refer to the two peaks as the π peak (low-energy feature) and the $\pi+\sigma$ peak (high-energy feature) throughout this paper.[61]

Another reason for differences between theory and experiment is contamination and beam-induced changes in the sample. Although very clean areas of the sample were selected, we have found that contamination tends to accumulate over time in the illuminated area, altering the EELS signal of the monolayer (see the SM,[54] Fig. S2). Additionally, the sample might degrade due to knock-on damage and other beam-induced processes.

B. G/MoS$_2$/G sandwich

With the knowledge of the simulated energy-loss functions of bare graphene and 1H-MoS$_2$ layers we now take a look at the experimental spectra of a graphene and MoS$_2$ heterostructure. In Fig. 1(b), measured energy-loss spectra of a G/MoS$_2$/G sandwich are compared to *ab initio* calculations for graphene

and MoS$_2$ monolayers for in-plane momentum transfers $\bar{q}$ of 0, 0.3, and $0.6\,\text{Å}^{-1}$ (ΓM direction). In the experiment, the sample was oriented along the ΓM direction of MoS$_2$, with an arbitrary orientation of the graphene layers. Due to the negligible in-plane anisotropy of both graphene and MoS$_2$ for up to $\bar{q} = 0.6\,\text{Å}^{-1}$ (see Ref. 12 and the Supplemental Material,[54] Fig. S4), we can assume the ΓM direction for all layers in our simulations.

From the comparison with the monolayer spectra, it is evident that low-loss spectra of the sandwich structure cannot be simply understood as a sum of its individual constituents like in the case of core-loss EELS. Indeed, the $\pi+\sigma$ peak of the G/MoS$_2$/G spectrum is always shifted to higher energy compared to the spectra of both graphene and MoS$_2$ and the relative height of the π peak is strongly decreased. Both effects can be attributed to Coulomb interactions between plasmons in different layers and have also been observed in low-loss spectra of multilayer graphene.[43,62] For a quantitative description of these interactions, rigorous calculations of the entire heterostructure are required.
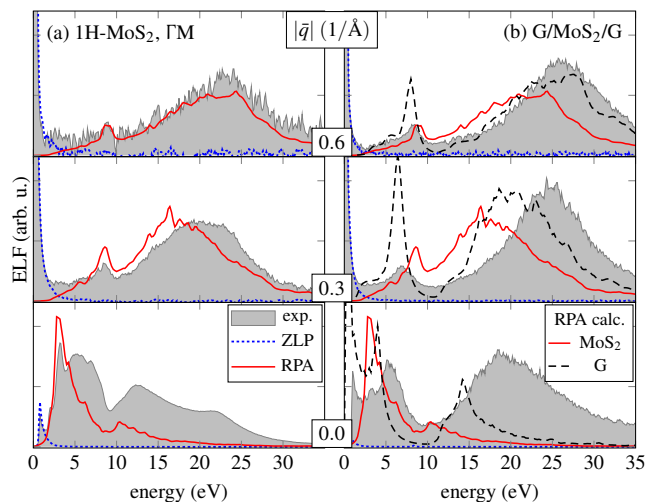

FIG. 1. (color online) Momentum-resolved energy-loss experiments on (a) 1H-MoS$_2$ monolayers and (b) G/MoS$_2$/G heterostructures for momentum transfers $\bar{q} = 0$, 0.3, and $0.6\,\text{Å}^{-1}$ along the ΓM direction of MoS$_2$. The measured energy-loss function (ELF, gray filled curve) is compared to corresponding *ab initio* RPA calculations of 1H-MoS$_2$ (red solid line) and graphene (black dashed line). Blue dotted curves indicate the background originating from unscattered electrons.

C. Model calculations

Brute-force TDDFT calculations for a stack of many layers with different lattice constants require large supercells with many atoms and thus a large computational effort even within RPA. At the same time, layers in van der Waals heterostructures are weakly bound and excitations on different sheets are mainly coupled via long-range Coulomb interactions. Neglecting interlayer hopping, we can therefore first perform

TDDFT calculations for each individual monolayer and include Coulomb interactions between neighboring sheets in a second step. In the following, we introduce corresponding model calculations of different complexity.

1. Building-block approach

In the framework of TDDFT, it appears natural to split the independent-particle polarizability χ^{KS} of the heterostructure into contributions $\chi^{KS,\alpha}$ of each individual monolayer α of the stack. Indeed $\chi^{KS,\alpha}$ is a very local quantity[63] which decays rapidly in the out-of-plane direction. Within the BBA,[64] the total KS polarizability of the stack is approximated as the sum over all monolayers located at height z_α. Given $\chi^{KS,\alpha}$ in mixed coordinates $(\bar{\boldsymbol{q}}, z)$, it reads

$$\chi^{KS}_{\bar{\boldsymbol{G}}\bar{\boldsymbol{G}}'}(\bar{\boldsymbol{q}}, E; z, z') \overset{BBA}{\approx} \sum_\alpha \chi^{KS,\alpha}_{\bar{\boldsymbol{G}}\bar{\boldsymbol{G}}'}(\bar{\boldsymbol{q}}, E; z - z_\alpha, z' - z_\alpha),$$

where the number, sequence, and distance of the layers can easily be varied without repeating a full TDDFT calculation. The microscopic density-response function $\chi_{\bar{\boldsymbol{G}}\bar{\boldsymbol{G}}'}(\bar{\boldsymbol{q}}, E; z, z')$ of the stack is then obtained by solving Eq. (2). In this step, long- and short-range Coulomb interactions are fully taken into account without any further approximation. Therefore, the BBA is very accurate. On the other hand, this approach is not appropriate for inverting the calculation and extracting the dielectric response of an unknown material from the EELS experiment of a stack. To this end, the full microscopic density-response matrix $\chi_{\bar{\boldsymbol{G}}\bar{\boldsymbol{G}}'}$ should be measured, not just a diagonal element as in Eq. (3). Additionally, lattice constants of different layers have to be commensurate such that corresponding in-plane reciprocal lattice vectors $\bar{\boldsymbol{G}}$ match between all summands in the above equation.

2. Layered electron-gas model

The computation can be simplified considerably by noting that the Coulomb potential of microscopic charge oscillations ($|\bar{\boldsymbol{G}}| > 0$) decays rapidly in the out-of-plane direction and thus hardly contributes to the coupling between different sheets. Thus, microscopic effects can be included in the response of each individual layer before multiple sheets are coupled via long-range Coulomb interactions. Within the LEG model,[38,65,66] this separation is achieved by introducing a dielectric model system of strictly two-dimensional, homogeneous sheets with polarizability $\Pi^\alpha(\bar{\boldsymbol{q}}, E)$ at vertical position z_α [Fig. 2(c)]. The microscopic polarizability of this stack of artificial layers is then a simple sum of yet unknown, scalar functions $\Pi^\alpha(\bar{\boldsymbol{q}}, E)$,

$$\pi^{LEG}_{\bar{\boldsymbol{G}}\bar{\boldsymbol{G}}'}(\bar{\boldsymbol{q}}, E; z, z') = \sum_\alpha \Pi^\alpha(\bar{\boldsymbol{q}} + \bar{\boldsymbol{G}}, E)\, \delta(z - z_\alpha)\delta(z' - z_\alpha)\delta_{\bar{\boldsymbol{G}}\bar{\boldsymbol{G}}'}.$$

The microscopic density response χ of this model system is obtained from Eq. (2), where χ^{KS} is replaced by π^{LEG}. As π^{LEG} is diagonal in $\bar{\boldsymbol{G}}$, the energy-loss function $ELF(\bar{\boldsymbol{q}}, E)$ of

the stack, given in Eq. (3), depends only on $\Pi^\alpha(\bar{\boldsymbol{q}}, E)$ inside the first Brillouin zone. To determine these unknown Π^α from first principles, we consider the LEG model for a single, isolated layer α.[43] In this case, Eq. (2) relates the polarizability $\Pi^\alpha(\bar{\boldsymbol{q}}, E)$ of the artificial layer to the macroscopic density response of the sheet $\bar{\chi}^\alpha(\bar{\boldsymbol{q}}, E) \equiv L_z\chi^\alpha_{00}(\bar{\boldsymbol{q}}, E)$,

$$\bar{\chi}^\alpha(\bar{\boldsymbol{q}}, E) = \Pi^\alpha(\bar{\boldsymbol{q}}, E) + \Pi^\alpha(\bar{\boldsymbol{q}}, E)\, v_{2D}(\bar{\boldsymbol{q}})\, \bar{\chi}^\alpha(\bar{\boldsymbol{q}}, E), \quad (4)$$

where $v_{2D} = 2\pi/\bar{q}$, denotes the Coulomb potential in two dimensions. Thus, Π^α can be obtained from a separate TDDFT calculation for each monolayer: First the microscopic response $\chi^{KS,\alpha}_{\boldsymbol{G}\boldsymbol{G}'}$ and $\chi^\alpha_{\boldsymbol{G}\boldsymbol{G}'}$ are computed, using mixed coordinates in Eq. (2). Then Eq. (4) is solved. By construction, the LEG model thus coincides with the TDDFT result for a single layer; that is, Π^α includes the averaged effect of all microscopic details. On the other hand, Π^α is just a scalar, macroscopic function and the lattice vectors of different layers do not need to be commensurate. Most importantly, the equations are simple enough to enable the reconstruction of the polarizability of an unknown layer.

3. In-plane homogeneous model

The main approximation of the LEG model is hidden in the assumption that all interlayer interactions can be modelled as interactions between strictly two-dimensional, homogeneous sheets. It breaks down, when some layers of the stack are thick or strongly inhomogeneous, i.e., when the interlayer distance is no longer large compared to the thickness or the in-plane lattice constant of the sheet. Several dielectric models for thick layers are currently being investigated in relation to Bethe-Salpeter calculations for monolayers and heterostructures using, e.g., homogeneous sheets of finite thickness[41,67–69] or multiple, infinitely thin sheets[70,71] for each individual layer. To extend the LEG model to thick layers, we propose to consider a heterostructure made of artificial layers α that are homogeneous in the in-plane direction and have an arbitrary, nonlocal behavior in the out-of-plane direction [Fig. 2(b)]. Within this in-plane homogeneous model (IPH), the microscopic polarizability of the stack is a sum of z-dependent polarizabilities $\tilde{\pi}^\alpha(\bar{\boldsymbol{q}}, E; z, z')$,

$$\pi^{IPH}_{\bar{\boldsymbol{G}}\bar{\boldsymbol{G}}'}(\bar{\boldsymbol{q}}, E; z, z') = \sum_\alpha \tilde{\pi}^\alpha(\bar{\boldsymbol{q}} + \bar{\boldsymbol{G}}, E; z - z_\alpha, z' - z_\alpha)\delta_{\bar{\boldsymbol{G}}\bar{\boldsymbol{G}}'}.$$

All other steps are completely analogous to the LEG model: The microscopic density response χ is obtained from Eq. (2), where χ^{KS} is replaced by π^{IPH}. Considering the IPH model for a single layer, the polarizability $\tilde{\pi}^\alpha(\bar{\boldsymbol{q}}, E; z, z')$ is obtained from the in-plane averaged density response $\chi^\alpha_{00}(\bar{\boldsymbol{q}}, E; z, z')$ using the analog of Eq. (4) for z-dependent polarizabilities. The effective polarizability $\tilde{\pi}^\alpha$ of the artificial layer is found to be, indeed, localized in the vertical direction, and heterostructures can be simply stacked along the z direction. Due to the homogeneity of the layers in the in-plane direction, we still avoid lattice-mismatch problems, but the inversion of the calculation becomes much more problematic.
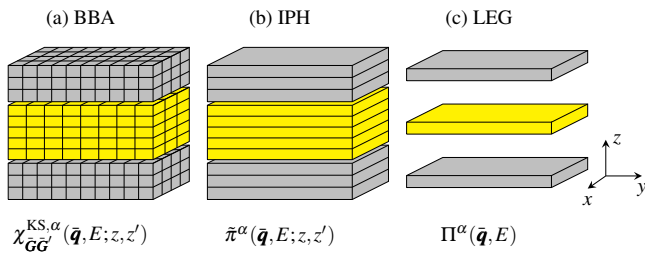
FIG. 2. Sketch of different model systems for a three-layer heterostructure (sandwich). (a) Fully microscopic description of the dielectric response including lattice mismatch within the building-block approach (BBA); (b) In-plane homogeneous (IPH) model with a z-dependent response for each layer. (c) Stack of strictly two-dimensional layers in the layered electron-gas (LEG) model.

4. Comparison of models for bulk MoS₂

As illustrated in Fig. 2, the complexity of the model decreases from BBA to IPH and the LEG model. At the same time, deviations from full *ab initio* results increase. To assess the accuracy of the presented models quantitatively, we discuss the prototypical examples of graphite and bulk MoS_2. For graphite and few-layer graphene, the LEG model has already proven useful for the accurate simulation of electron energy-loss spectra in the low-loss region.[42,43] For in-plane momentum transfers, all three model calculations give nearly the same result. This is no longer the case for heterostructures with thick sheets. In bulk MoS_2, the layer thickness $d_S = 3.2\,Å$, which can be estimated by the distance between upper and lower sulfur atoms, is half the interlayer distance $d = 6.15\,Å$. To evaluate the performance of the model calculations for bulk MoS_2, we compare momentum-resolved EELS measurements for an intermediate momentum transfer $\bar{q} = 0.3\,Å^{-1}$ along the ΓM direction with corresponding simulations (see Fig. 3). As a reference, the result of a standard TDDFT-RPA calculation is shown as a black solid line. It is found to be in very good agreement with the experiment. The BBA calculation (green solid line), which neglects only interlayer hopping, gives nearly the same spectrum as the RPA calculation. Very similar results are obtained if the individual monolayers are approximated as homogeneous sheets with variation along the z direction (IPH calculation, blue dash-dotted line). However, the LEG model clearly fails (red dashed line); that is, the approximation of the MoS_2 sheets as homogeneous, strictly two-dimensional layers does not hold.

Instead of comparing systems with different monolayer thicknesses, like graphite and MoS_2, we can artificially increase the interlayer distance to show that the finite thickness of the layers is the reason for the failure of the LEG model. Indeed, the ratio between the z extension and interlayer distance is the important parameter. In the inset in Fig. 3, we consider the $\pi+\sigma$ peak position[54] for artificial bulk MoS_2 with an increased interlayer distance. Independent of the model, the peak energy decreases with increasing layer distance and approaches the value of an isolated MoS_2 monolayer in the limit $d \to \infty$. This can be explained by the decreasing Coulomb
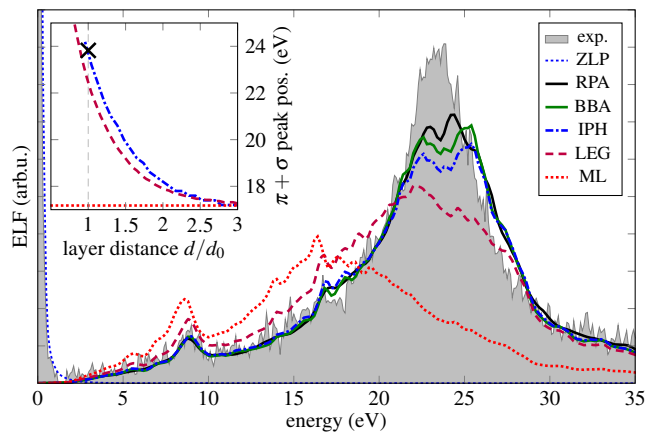

FIG. 3. (color online) Validation of different model calculations for EEL spectra of bulk MoS_2 at in-plane momentum transfer $\bar{q} = 0.3\,Å^{-1}$ along the ΓM direction: Comparison between BBA, IPH, and LEG models (green solid, blue dash-dotted, and red dashed lines, respectively). As a reference, a full TDDFT calculation (RPA; black solid line) and the measured EEL spectrum (gray filled curve) are shown. Additionally, the RPA spectrum for a single MoS_2 monolayer is shown (red dotted line). The inset shows the calculated position of the $\pi+\sigma$ peak in bulk MoS_2 with an artificially increased layer distance d. The result of the rigorous RPA calculation for bulk MoS_2 (black cross) can be reproduced by model calculations, only if the z dependence of the monolayers is considered (IPH; blue dash-dotted line).

interaction between neighboring sheets. On the other hand, the LEG model (red dashed line) systematically underestimates the $\pi+\sigma$ peak position, which corresponds to an underestimation of the Coulomb interaction compared to the IPH model (blue dash-dotted line) or the reference TDDFT calculation (black cross). The error of the LEG model is as large as $1.6\,eV$ in the $\pi+\sigma$ peak position at bulk interlayer distance $d = d_0$. This error decreases for larger d, i.e., when the z extension of the layers becomes less important.

Our comparison of the different models shows that the IPH model is able to correctly describe Coulomb interactions in heterostructures even for thick layers, while the LEG model fails in this case. The calculated EEL spectra are nearly identical to full TDDFT calculations in RPA. On the other hand, IPH and LEG models both include microscopic inhomogeneities only implicitly via an effective dielectric constant. This allows us to easily combine arbitrary 2D layers even with incommensurable unit cells. The IPH model is thus ideal for simulating the in-plane dielectric response of 2D heterostructures with arbitrary stacking.

D. Calculations for the G/MoS₂/G heterostructure

Having established an accurate and fast method to simulate in-plane EEL spectra of arbitrary heterostructures, we now revisit our experimental results for the G/MoS₂/G sandwich samples discussed in Section III B. We focus on intermediate momentum transfers $\bar{q} = 0.3\,Å^{-1}$, where differences between
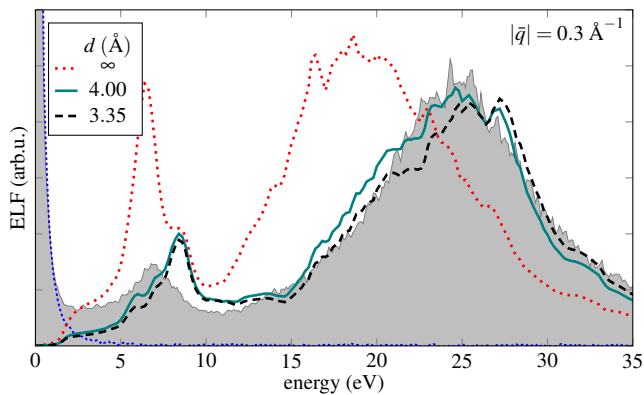
FIG. 4. (color online) Variation of the interlayer distance d in the G/MoS$_2$/G sandwich structure. Experimental EEL spectra (gray filled curve) for a momentum transfer of $\bar{q} = 0.3\,\text{Å}^{-1}$ are compared to IPH model calculations for $d = 3.35\,\text{Å}$, $d = 4.0\,\text{Å}$, and $d \to \infty$.

FIG. 5. (color online) Comparison of experimental EEL spectra (gray filled curve) of the G/MoS$_2$/G sandwich structure with corresponding IPH and LEG model calculations for a momentum transfer of $\bar{q} = 0.3\,\text{Å}^{-1}$ and an interlayer distance $d = 4.95\,\text{Å}$ (see text).

sandwich and monolayer spectra are very pronounced [see Fig. 1(b)] and RPA calculations have been proven to describe our experimental results for individual monolayers sufficiently well [see Fig. 1(a)]. Thus, calculations using the IPH model can be directly compared to our EELS measurements.

Unfortunately, the interlayer distance d between graphene and 1H-MoS$_2$ layers in the G/MoS$_2$/G sandwich is not known *a priori*. Very few theoretical estimations exist in the literature, using molecular dynamics simulations[72] or DFT calculations.[73,74] Experimentally, the layer distance is hard to measure, and it might even vary if contamination is trapped between the layers during the assembly of the sandwich. We therefore consider different layer distances d ranging between two limiting cases (see Fig. 4): As the upper bound, we consider infinitely separated layers ($d \to \infty$), where the coupling between different sheets vanishes and the simulated EEL signal becomes a simple sum of graphene and 1H-MoS$_2$ spectra (red dotted line). As the lower bound, we use the interlayer distance of bulk graphite ($d = 3.35\,\text{Å}$) ignoring the increased thickness of the sandwiched MoS$_2$ layer compared to graphene. Although the Coulomb interaction between different layers is overestimated in this case, the overall agreement with our experimental results is largely improved (black dashed line). This shows the importance of the Coulomb coupling, which has two main effects on the energy-loss spectra: First, the π peak is strongly suppressed in comparison to a simple sum of the graphene and 1H-MoS$_2$ spectra. Second, the π and $\pi+\sigma$ peaks are shifted to higher energies when the Coulomb coupling increases, i.e., d decreases. This is the same behavior as observed in bulk MoS$_2$ (see Fig. 3) or graphite.

Using the sensitivity of the $\pi+\sigma$ peak position to the interlayer distance d, we can try to estimate d by matching the calculated peak position to our experimental results. The best fit result for the IPH model is obtained at an interlayer distance d of about 4.0 Å (green solid line). This value is much smaller than predictions from theory suggest. The given carbon-sulfur distances in Refs. 72–74 are on the order of the interlayer distance of graphite and would result in a distance d of around
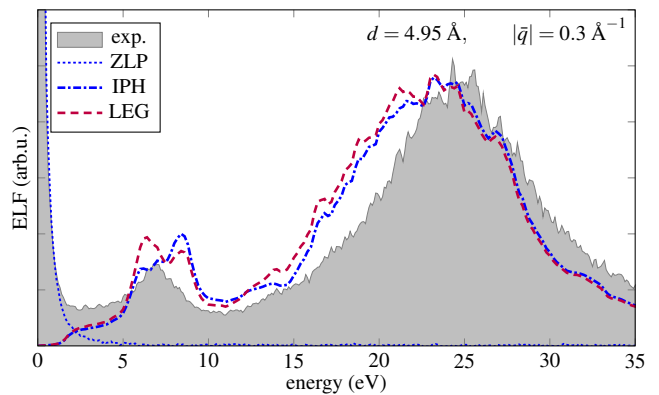
4.95 Å.[75] The large difference between these layer distances suggests that the fitted distance d compensates discrepancies between experimental and theoretical results of different origins. In particular, it has to be noted that for the best match of the $\pi+\sigma$ peak, the energy of the π peak is overestimated by about 1.5 eV by the calculation.

So far, we have assumed that the polarizabilities of both graphene and monolayer MoS$_2$ are known, and we considered the layer distance d to be the (only) unknown parameter. If we now come back to our initial aim of reconstructing the polarizability of monolayer MoS$_2$ from the G/MoS$_2$/G spectrum, we have to refer to the literature value of $d = 4.95\,\text{Å}$. For this fixed layer distance, the resulting EEL spectrum calculated using the IPH model is shown in Fig. 5 (blue dash-dotted line). Moreover, we revive the less complicated LEG model which can in principle be used for an inverse calculation, i.e., the reconstruction of the polarizability of 1H-MoS$_2$. Using the same layer distance, a LEG calculation for G/MoS$_2$/G (red dashed line) yields nearly the same result as the IPH model. In contrast to the case of bulk MoS$_2$ we find that for the G/MoS$_2$/G sandwich structure, the LEG still matches our IPH reference calculation. This implies that the sandwiching approach for reduced beam damage could work.

For a practical implementation, however, there are many pitfalls. In the following, we want to summarize the main complications in experiments and theory. First, as already mentioned in Sec. III A, there are multiple possible reasons for the mismatch between experiments and simulations. From the theoretical point of view, neglecting exchange and correlation effects in the theoretical description of MoS$_2$ leads to differences at smaller momentum transfers $\bar{q}$. Moreover, the simulations should also account for the finite q resolution in the EELS measurements. In TEM experiments, electron-beam-induced modifications of the sample can alter the spectra as well as (hydrocarbon) contamination (see the Supplemental Material,[54] Fig. S2). Even the number of layers can vary over the sample and is hard to assess in a TEM experiment. Exact methods based on electron diffraction exist only for cer-

tain cases, e.g., to distinguish between monolayer and bilayer graphene and between 1H and 2H-MoS$_2$.[76,77] In particular for the application of the encapsulation approach to an unknown 2D material, this can pose a serious limitation together with the unknown interlayer distances.

Last, before the polarizabilities of the monolayers can be separated, the complex inverse dielectric function ε^{-1} of the sandwich structure needs to be determined via Kramers-Kronig analysis. This requires a very precise subtraction of the zero-loss peak and may be complicated by retardation effects.[78] It should be noted that this is a particular problem for low-energy excitations in the range of several electronvolts. But even for core-loss spectra, which can be generally understood as a simple sum of contributions from different monolayers in a first approximation, the sandwiching of the sample might alter the near-edge spectra which contain information about excitations in the valence region.

tions for bulk MoS$_2$. This offers an accurate and fast method to simulate the EELS signal of arbitrary heterostructures which can be directly compared to experimental results.

Using these IPH calculations as a reference, we have investigated the dielectric response of a G/MoS$_2$/G sandwich. In this case, the LEG model was found to give a rather good description of the EELS signal. On this basis, it is, in principle, possible to extract the polarizability of a bare MoS$_2$ monolayer from the EELS signal of the less beam sensitive G/MoS$_2$/G sandwich if the polarizability of graphene is known. For a practical implementation of this sandwiching technique in low-loss EELS, several experimental difficulties arise which have been discussed in detail. In particular, the strong dependence of the results on the unknown interlayer separation was found to be critical. Hence, our results emphasize the need for low-voltage microscopy in a very clean environment to enable precise measurements of EEL spectra of monolayers.

IV. CONCLUSIONS

In this paper, different dielectric models for the calculation of low-loss EEL spectra of prototypical heterostructures have been assessed by comparison with *ab initio* calculations and momentum-resolved EELS measurements. Using bulk MoS$_2$ as a test system, we have shown that the commonly used layered electron-gas model might fail for a stack of thick layers. The origin of this failure is the neglect of the finite extent of each individual 1H-MoS$_2$ sheet in the out-of-plane direction ($d_S \approx 3.2\,\text{Å}$), which leads to an underestimation of the Coulomb interaction between neighboring layers. We have introduced a partly microscopic, in-plane homogeneous model, which takes the finite layer thickness into account and shows nearly perfect agreement with rigorous TDDFT-RPA calcula-

* michael.mohn@uni-ulm.de
1 T. Pichler, M. Knupfer, M. S. Golden, J. Fink, A. Rinzler, and R. E. Smalley, Phys. Rev. Lett. 80, 4729 (1998).
2 J. A. Soininen and E. L. Shirley, Physical Review B 61, 16423 (2000).
3 P. Cudazzo, L. Sponza, C. Giorgetti, L. Reining, F. Sottile, and M. Gatti, Physical Review Letters 116, 066803 (2016).
4 R. B. Pettit, J. Silcox, and R. Vincent, Physical Review B 11, 3116 (1975).
5 C. H. Chen, J. Phys. C: Solid State Phys. 9, L321 (1976).
6 R. Arenal, M. Kociak, and N. J. Zaluzec, Applied Physics Letters 90, 204105 (2007), https://doi.org/10.1063/1.2740185.
7 F. Fossard, L. Sponza, L. Schué, C. Attaccalite, F. Ducastelle, J. Barjon, and A. Loiseau, Physical Review B 96, 115304 (2017).
8 C. Kramberger, R. Hambach, C. Giorgetti, M. H. Rümmeli, M. Knupfer, J. Fink, B. Büchner, L. Reining, E. Einarsson, S. Maruyama, F. Sottile, K. Hannewald, V. Olevano, A. G. Marinopoulos, and T. Pichler, Physical Review Letters 100, 196803 (2008).
9 C. Colliex, M. Kociak, and O. Stéphan, Ultramicroscopy 162, A1 (2016).
10 F. S. Hage, T. P. Hardcastle, A. J. Scott, R. Brydson, and Q. M. Ramasse, Physical Review B 95, 195411 (2017).
11 M. K. Kinyanjui, C. Kramberger, T. Pichler, J. C. Meyer, P. Wachsmuth, G. Benner, and U. Kaiser, Europhysics Letters 97, 57005 (2012).
12 P. Wachsmuth, R. Hambach, M. K. Kinyanjui, M. Guzzo, G. Benner, and U. Kaiser, Phys. Rev. B 88, 075433 (2013).
13 S. C. Liou, C.-S. Shie, C. H. Chen, R. Breitwieser, W. W. Pai, G. Y. Guo, and M.-W. Chu, Phys. Rev. B 91, 045418 (2015).
14 J. Hong, C. Li, C. Jin, X. Zhang, Z. Zhang, and J. Yuan, Physical Review B 93, 075440 (2016).
15 H. C. Nerl, K. T. Winther, F. S. Hage, K. S. Thygesen, L. Houben, C. Backes, J. N. Coleman, Q. M. Ramasse, and V. Nicolosi, npj 2D Materials and Applications 1, 2 (2017).
16 J. C. Meyer, F. Eder, S. Kurasch, V. Skalakova, J. Kotakoski, H. J. Park, S. Roth, A. Chuvilin, S. Eyhusen, G. Benner, A. V. Krasheninnikov, and U. Kaiser, Physical Review Letters 108, 196102 (2012).
17 J. Kotakoski, C. H. Jin, O. Lehtinen, K. Suenaga, and A. V. Krasheninnikov, Physical Review B 82, 113404 (2010).
18 H. P. Komsa, J. Kotakoski, S. Kurasch, O. Lehtinen, U. Kaiser, and A. V. Krasheninnikov, Physical Review Letters 109, 035503

(2012).

[19] D. C. Bell, C. J. Russo, and G. Benner, Microscopy and Microanalysis **16**, 386 (2010).

[20] T. Sasaki, H. Sawada, F. Hosokawa, Y. Kohno, T. Tomita, T. Kaneyama, Y. Kondo, K. Kimoto, Y. Sato, and K. Suenaga, Journal of Electron Microscopy **59**, 7 (2010).

[21] U. Kaiser, J. Biskupek, J. C. Meyer, J. Leschner, L. Lechner, H. Rose, M. Stöger-Pollach, A. N. Khlobystov, P. Hartel, H. Müller, M. Haider, S. Eyhusen, and G. Benner, Ultramicroscopy **111**, 1239 (2011).

[22] D. C. Bell, C. J. Russo, and D. V. Kolmykov, Ultramicroscopy **114**, 31 (2012).

[23] G. Algara-Siller, S. Kurasch, M. Sedighi, O. Lehtinen, and U. Kaiser, Applied Physics Letters **103**, 203107 (2013).

[24] R. Zan, Q. M. Ramasse, R. Jalil, T. Georgiou, U. Bangert, and K. S. Novoselov, ACS Nano **7**, 10167 (2013).

[25] Z. Lee, K.-J. Jeon, A. Dato, R. Erni, T. J. Richardson, M. Frenklach, and V. Radmilovic, Nano Letters **9**, 3365 (2009).

[26] A. K. Geim and I. V. Grigorieva, Nature **499**, 419 (2013), 1307.6718.

[27] S. J. Haigh, A. Gholinia, R. Jalil, S. Romani, L. Britnell, D. C. Elias, K. S. Novoselov, L. A. Ponomarenko, A. K. Geim, and R. Gorbachev, Nature Materials **11**, 764 (2012).

[28] L. Britnell, R. M. Ribeiro, A. Eckmann, R. Jalil, B. D. Belle, A. Mishchenko, Y.-J. Kim, R. V. Gorbachev, T. Georgiou, S. V. Morozov, A. N. Grigorenko, A. K. Geim, C. Casiraghi, A. H. C. Neto, and K. S. Novoselov, Science **340**, 1311 (2013).

[29] M. Velick and P. S. Toth, Applied Materials Today **8**, 68 (2017).

[30] W. Aggoune, C. Cocchi, D. Nabok, K. Rezouali, M. Akli Belkhir, and C. Draxl, The Journal of Physical Chemistry Letters **8**, 1464 (2017).

[31] L. Britnell, R. V. Gorbachev, R. Jalil, B. D. Belle, F. Schedin, A. Mishchenko, T. Georgiou, M. I. Katsnelson, L. Eaves, S. V. Morozov, N. M. R. Peres, J. Leist, A. K. Geim, K. S. Novoselov, and L. A. Ponomarenko, Science **335**, 947 (2012).

[32] F. Withers, O. Del Pozo-Zamudio, A. Mishchenko, A. P. Rooney, A. Gholinia, K. Watanabe, T. Taniguchi, S. J. Haigh, A. K. Geim, A. I. Tartakovskii, and K. S. Novoselov, Nature Materials **14**, 301 (2015).

[33] B. V. Lotsch, Annual Review of Materials Research **45**, 85 (2015).

[34] K. S. Novoselov, A. Mishchenko, A. Carvalho, and A. H. Castro Neto, Science **353** (2016), 10.1126/science.aac9439.

[35] H. Sahin, E. Torun, C. Bacaksiz, S. Horzum, J. Kang, R. T. Senger, and F. M. Peeters, Wiley Interdisciplinary Reviews: Computational Molecular Science **6**, 351 (2016).

[36] K. S. Thygesen, 2D Materials **4**, 022004 (2017).

[37] Z. Torbatian and R. Asgari, Applied Sciences **8**, 238 (2018).

[38] A. L. Fetter, Ann. Phys. (NY) **88**, 1 (1974).

[39] K. Andersen, S. Latini, and K. S. Thygesen, Nano Lett. **15**, 4616 (2015).

[40] J. Koskelo, G. Fugallo, M. Hakala, M. Gatti, F. Sottile, and P. Cudazzo, Physical Review B **95**, 035125 (2017).

[41] M. L. Trolle, T. G. Pedersen, and V. Véniard, Scientific Reports **7**, 39844 (2017).

[42] V. B. Jovanović, I. Radović, D. Borka, and Z. L. Misković, Phys. Rev. B. **84**, 155416 (2011).

[43] P. Wachsmuth, R. Hambach, G. Benner, and U. Kaiser, Phys. Rev. B **90**, 235434 (2014).

[44] P. Wachsmuth, *Momentum-resolved electron energy-loss spectroscopy of graphene*, Ph.D. thesis, Universität Ulm, Ulm (2014).

[45] R. Hambach and P. Wachsmuth, "TEMareels scripts on GitHub, https://github.com/rhambach/TEMareels," .

[46] S. Botti, A. Schindlmayr, R. D. Sole, and L. Reining, Reports Prog. Phys. **70**, 357 (2007).

[47] X. Gonze, B. Amadon, P. M. Anglade, J. M. Beuken, F. Bottin, P. Boulanger, F. Bruneval, D. Caliste, R. Caracas, M. Côté, T. Deutsch, L. Genovese, P. Ghosez, M. Giantomassi, S. Goedecker, D. R. Hamann, P. Hermet, F. Jollet, G. Jomard, S. Leroux, M. Mancini, S. Mazevet, M. J. T. Oliveira, G. Onida, Y. Pouillon, T. Rangel, G. M. Rignanese, D. Sangalli, R. Shaltaf, M. Torrent, M. J. Verstraete, G. Zerah, and J. W. Zwanziger, Comput. Phys. Commun. **180**, 2582 (2009).

[48] V. Olevano, L. Reining, and F. Sottile, "dp-code, http://www.dp-code.org/," (1998).

[49] Z. Yuan and S. Gao, Comput. Phys. Commun. **180**, 466 (2009).

[50] M. Pisarra, A. Sindona, M. Gravina, V. M. Silkin, and J. M. Pitarke, Phys. Rev. B **93**, 035440 (2016).

[51] Y. Gao and Z. Yuan, Solid State Communications **151**, 1009 (2011).

[52] V. Despoja, D. Novko, K. Dekanić, M. Šunjić, and L. Marušić, Physical Review B **87**, 075447 (2013).

[53] V. Despoja, Z. Rukelj, and L. Marušić, Phys. Rev. B **94**, 165446 (2016).

[54] See Supplemental Material at http://link.aps.org/supplemental/10.1103/PhysRevB.97.235410 for our full data on MoS_2 monolayers and details on contamination, the finite-aperture effect, and how to extract the $\pi+\sigma$ peak position.

[55] L. H. G. Tizei, Y. C. Lin, M. Mukai, H. Sawada, A. Y. Lu, L. J. Li, K. Kimoto, and K. Suenaga, Physical Review Letters **114**, 107601 (2015).

[56] L. H. G. Tizei, Y.-C. Lin, A.-Y. Lu, L.-J. Li, and K. Suenaga, Applied Physics Letters **108**, 163107 (2016).

[57] Y. Yu, Y. Yu, Y. Cai, W. Li, A. Gurarslan, H. Peelaers, D. E. Aspnes, C. G. Van De Walle, N. V. Nguyen, Y. W. Zhang, and L. Cao, Scientific Reports **5**, 16996 (2015).

[58] A. Molina-Sánchez, D. Sangalli, K. Hummer, A. Marini, and L. Wirtz, Physical Review B **88**, 045412 (2013).

[59] D. Y. Qiu, F. H. da Jornada, and S. G. Louie, Physical Review B **93**, 235435 (2016).

[60] D. Y. Qiu, T. Cao, and S. G. Louie, Physical Review Letters **115**, 176801 (2015).

[61] W. Y. Liang and S. L. Cundy, The Philosophical Magazine: A Journal of Theoretical Experimental and Applied Physics **19**, 1031 (1969).

[62] T. Eberlein, U. Bangert, R. R. Nair, R. Jones, M. Gass, A. L. Bleloch, K. S. Novoselov, A. Geim, and P. R. Briddon, Physical Review B **77**, 233406 (2008).

[63] C. Brouder, G. Panati, M. Calandra, C. Mourougane, and N. Marzari, Phys. Rev. Lett. **98**, 046402 (2007).

[64] R. Hambach, *Theory and ab-initio calculations of collective excitations in nanostructures: towards spatially-resolved EELS*, Ph.D. thesis, Ecole Polytechnique, Palaiseau, France (2010).

[65] S. Das Sarma and J. Quinn, Phys. Rev. B **25**, 7603 (1982).

[66] W. L. Bloss and E. M. Brody, Solid State Commun. **43**, 523 (1982).

[67] P. Cudazzo, I. V. Tokatly, and A. Rubio, Physical Review B **84**, 085406 (2011).

[68] S. Latini, T. Olsen, and K. S. Thygesen, Phys. Rev. B **92**, 245123 (2015).

[69] L. Meckbach, T. Stroucken, and S. W. Koch, Physical Review B **97**, 035425 (2018).

[70] B. Scharf, D. Van Tuan, I. Žutić, and H. Dery, arXiv:1801.06217 [cond-mat] (2018), arXiv:1801.06217 [cond-mat].

[71] D. Van Tuan, M. Yang, and H. Dery, arXiv:1801.00477 [cond-mat] (2018), arXiv:1801.00477 [cond-mat].

[72] J.-W. Jiang and H. S. Park, Applied Physics Letters **105**, 033108 (2014).

[73] Y. Ma, Y. Dai, M. Guo, C. Niu, and B. Huang, Nanoscale **3**, 3883 (2011).

[74] Z. Šljivančanin and M. Belić, Phys. Rev. Materials **1**, 044003 (2017).

[75] In our calculations, we always refer to the C-Mo distance as the interlayer distance d.

[76] J. C. Meyer, A. K. Geim, M. I. Katsnelson, K. S. Novoselov, T. J. Booth, and S. Roth, Nature **446**, 60 (2007).

[77] J. Brivio, D. T. L. Alexander, and A. Kis, Nano Letters **11**, 5148 (2011).

[78] M. Stöger-Pollach, H. Franco, P. Schattschneider, S. Lazar, B. Schaffer, W. Grogger, and H. Zandbergen, Micron **37**, 396 (2006).